Simple design of 2 kW Yb-doped fiber laser

Weixuan Lin[a,b,c], Maxime Desjardins-Carrière[b], Victor Lambin Iezzi[b], André Vincelette[b], Marie-Hélène Bussières-Hersir[b], Martin Rochette[a]

[a]*Department of Electrical and Computer Engineering, McGill University, Montréal, Québec, Canada*
[b]*ITF Technologies, 400 boul. Montpellier, Montréal, Québec, Canada*
[c]*weixuan.lin@mail.mcgill.ca*

Abstract

We report a simple design of Yb-doped fiber laser providing a record output power of 2 kW and power conversion efficiency of 68%. The high output power of this unamplified laser oscillator is obtained thanks to the suppression of Raman emission over a spectral range of 21 nm from chirped and tilted fiber Bragg gratings inside the gain fiber of the laser oscillator. The laser design is based on optical components that are commercially widespread and low-cost, such as 20 μm-core double-cladding active and passive fibers, as well as pump laser diodes at a wavelength of 915 nm. The performance of this laser is evaluated in terms of output power, power conversion efficiency, and thermal dissipation. A numerical model that serves to determine the optimal experimental configuration is also provided.

Keywords: High power fiber lasers, stimulated Raman scattering, chirped and tilted fiber Bragg grating

1. Introduction

Continuous-wave high power Yb-doped fiber lasers (YDFL) operating at an output wavelength ~1100 nm are widely used for industrial metal processing such as cutting, drilling, welding, and cleaning [1]. YDFLs based on double-cladding YDFs with a core diameter of 20 μm and a cladding diameter of 400 μm (20/400 μm) have been reported with an output power in excess of 1 kW since 2012 [2]. Figure 1a) depicts the geometry of a 20/400 μm YDF. A first advantage of the 400 μm cladding diameter is that it enables more pump light to be injected in the cladding, compared to other commercial YDFs with smaller cladding diameters such as 10/125 μm and 14/250 μm. Second, the 20 μm core diameter leads to better robustness against high-order mode propagation than 25/400 μm and 30/400 μm YDFs, which in return leads to better beam quality. A non wavelength stabilized (non-WS) laser diode is another component that is widespread in industrial products and that can be used advantageously for the pumping of YDFs. Figure 1b) shows typical absorption and emission cross sections of YDFs [3]. Comparing absorption peaks at wavelengths of 915 nm and 976 nm, the peak at 915 nm is characterized by a broad spectral width of ~21 nm at 90% from the maximum in comparison with the peak of 976 nm with a width of ~3 nm at 90% from the maximum. Despite being attractive because of the high level of absorption, pumping at a wavelength of 976 nm however has its drawbacks. First, high absorption rates have been associated to photo-darkening, which is a deleterious effect that limits the power conversion efficiency and lifetime of YDFs [4, 5]. Second, pumping at a a wavelength of 976 nm requires wavelength stabilized (WS) pump laser diodes for practical implementation, since a wavelength drift of 1-2 nm is sufficient to impair the pumping efficiency [6]. The stabilization mechanism behind WS laser diodes consists into volume Bragg gratings or fiber Bragg gratings [7, 8, 9, 10, 11], thereby increasing the cost of WS laser diodes by a factor of ~4 with respect to non-WS laser diodes. In contrast, non-WS laser diodes suffice to accommodate the broad absorption peak of 915 nm, thereby offering the advantage of simplicity and low cost. Therefore, notwithstanding that YDFLs based on 20/400 μm YDFs and WS laser diodes at a wavelength of 976 nm have led to output power of >2 kW [12, 13] and even >3 kW [14], YDFLs that make use of non-WS pump sources at a wavelength of 915 nm are of utmost industrial interest thanks to their simplicity, low-cost, as well as the ease of thermal dissipation management they provide.

With the use of commercially widespread components such as 20/400 μm YDFs and non-WS laser diodes at a wavelength of 915 nm, the output power of YDFLs has been limited to 1.5 kW because of stimulated Raman

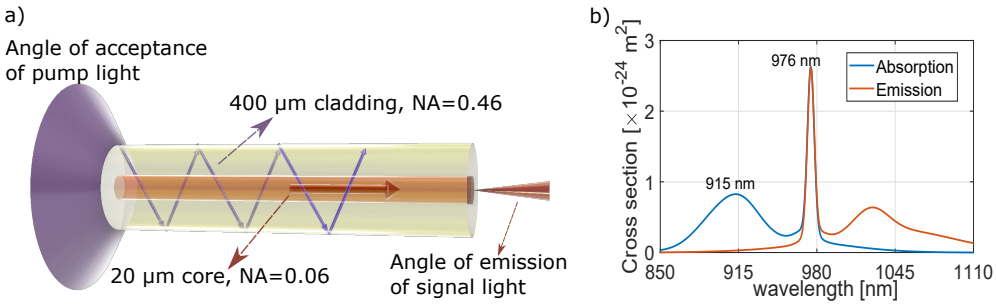

Figure 1: a) Geometry of 20/400 µm YDF (not to scale). b) Typical absorption and emission cross sections of YDF.

scattering (SRS) [15]. With the onset of SRS, a substantial fraction of laser power at the emission wavelength of 1080 nm is spectrally offset by 13.2 THz towards longer wavelengths, thereby leading to an SRS peak at a wavelength of 1135 nm. The more the fraction of SRS power to laser power (i.e. Raman ratio) exceeds 1%, the more the beam output quality degrades [16, 17]. Increasing the power of YDFLs thus requires the suppression of SRS. Typical approaches to mitigate SRS include increasing the output-coupler bandwidth in the oscillator section of a master-oscillator power amplifier (MOPA) [18], decreasing the coil diameter of gain fibers [19], and optimizing injected seed power in a MOPA [20]. In recent years, wideband-rejection filters have been developed from chirped and tilted fiber Bragg gratings (CTFBG) [18, 21], which have been successfully tested and validated in YDFLs [22, 23, 24]. In a previous work, we have improved the output power of a YDFL from 1.54 kW to 1.8 kW, by inserting a CTFBG in the gain fiber of the resonant cavity [24]. However, SRS light was leaking from both filtering band edges of the 10 nm wide CTFBG, limiting the efficiency of SRS suppression [24]. In this paper, we use a cascade of CTFBGs in the gain fiber of a laser oscillator to efficiently suppress SRS and raise the output YDFL power up to 2.03 kW. The CTFBGs suppress SRS by up to 16 dB over a spectral width of 21 nm. The performance of this laser is evaluated in terms of output power, power conversion efficiency, and thermal dissipation. The numerical model that serves to determine the optimal experimental configuration is also provided. The YDFL design comprises 20/400 µm YDFs and non-WS laser diodes at a wavelength of 915 nm. This simple design of unamplified YDFL cavity is thus of utmost interest for industrial applications.

2. Experimental configuration

One of the effective methods to broaden the filtering band of a Raman filter is to cascade CTFBGs with mismatched central wavelengths [25, 26]. The Raman filter used in this experiment is a cascade of two CTFBGs written in a single 20/400 µm Ge-doped fiber (GDF), with numerical aperture of 0.06/0.46, respectively for the core/cladding. The CTFBGs are written by using standard UV writing through a phase-mask, with a writing setup similar to the one of Ref. 21. Figure 2 schematize the cascade of CTFBGs. The two CTFBGs have an optimized tilt angle of $4^\circ \pm 0.1^\circ$ to enable a strong core-to-clad reflection while minimizing core-to-core reflection [27]. Figure 3 shows the transmission and reflection spectra of the cascaded CTFBGs. The cascade comprises CTFBG1 that is centered at the central wavelength of 1140 nm, followed by CTFBG2 centered at the central wavelength of 1130 nm. The assembly leads to a notch filter with a depth of 16 dB and a 10 dB bandwidth of 21.1 nm centered at a wavelength of 1135 nm, thus covering the SRS emission spectrum from 1125.5 nm to 1146.6 nm. The transmission loss of the assembly is 0.12 dB at a wavelength of 1080 nm. The two CTFBGs are aligned in an order such that SRS light passes through CTFBG1 before passing through CTFBG2. As well, the chirp of both CTFBGs is such that SRS light enters from their long-period ends. With this order, the Bragg reflection (i.e., incident LP_{01} mode to reflected LP_{01} mode) from CTFBG2 is filtered by CTFBG1, while the Bragg reflection from CTFBG1 is mismatched from the SRS spectral range. Hence, this design of cascaded CTFBGs set a broad filtering band and effectively eliminates most of the Bragg reflection at the same time. Compared to a single CTFBG with a 10 dB bandwidth 10 nm [24], the cascaded CTFBGs enable a sufficient filtering coverage over the SRS spectral range. Also from Fig. 3, the Bragg reflection from the cascaded CTFBGs has a -38 dB peak at a wavelength of 1150.0 nm, leading to a negligible overlap with the SRS spectral range.

This is an important detail since it has been reported that Bragg reflection of a CTFBG can reflect SRS light back into the laser that subsequently results into a strong forward SRS light [24, 28].

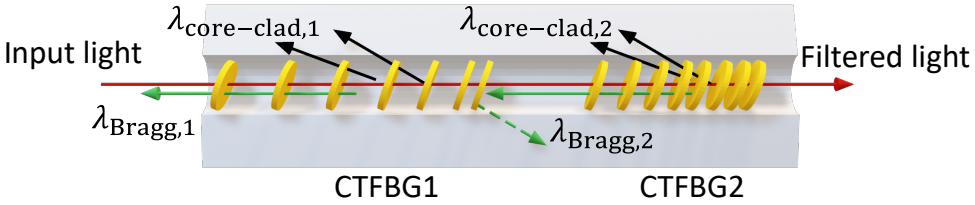

Figure 2: Schematic of the cascaded CTFBGs. CTFBG1 is centered at a wavelength of 1140 nm whereas CTFBG2 is centered at a wavelength of 1130 nm. $\lambda_{\text{core-clad}}$: core-to-clad reflection by a CTFBG. λ_{Bragg}: Bragg reflection by a CTFBG.

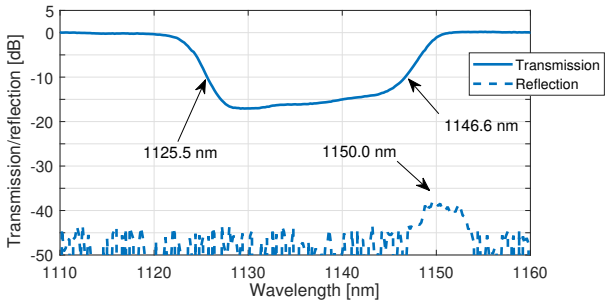

Figure 3: Transmission and reflection spectral profiles of the cascaded CTFBGs.

Figure 4 shows a schematic of the YDFL, which consists of 18 non-WS pump laser diodes at the wavelength of 915 nm, an 18-port fiber bundle combiner, a high-reflection (HR) FBG (99%, at 1080 nm), gain fiber, an SRS filter, and an output-coupler (OC) FBG (10%, at 1080 nm). The gain fibers are 20/400 µm YDFs (Coherent LMA-YDF-20/400-M) with an absorption rate of 0.4 dB/m at the wavelength of 915 nm. The laser output is sent to a cladding-light stripper (CLS) for residual pump light removal and a 7 m long 20/400 µm GDF followed by a quartz block head is used for beam delivery. The CTFBG cascade subdivides the 40 m long gain fiber of the cavity into two segments X m and (40-X) m, where X is a variable that is changed for optimization. The CTFBG in inserted by fusion splicing of YDF with GDF fiber, with an insertion loss of 0.1 dB for each splice. In the active fiber, SRS power increases gradually in the forward direction. As a result, a later insertion of the CTFBG filters is beneficial to maximize the Raman ratio, but also leads to a decrease in the power conversion efficiency of the YDFL. A numerical modelling is conducted in the next section to compare the performance of various value of X.

3. Optimization of the insertion position of the CTFBG

This section presents a simulation model used to determine the optimal insertion position of the CTFBG inside a 40 m long YDF oscillator. The model follows the same framework in Ref. 29, adapted to include the SRS filter placed inside the gain fiber.

3.1. Numerical modelling

The model is based on nonlinear Schrodinger equations (NLSE) with gain, dispersion, and nonlinear terms [29]. It numerically simulates the amplification process of forward and backward propagating fields. The fields are described as complex amplitudes in time domain $A^{\pm}(z,t)$ and frequency domain $\tilde{A}^{\pm}(z,\omega)$, where + refers to forward propagation and − refers to backward propagation with respect to the laser output direction. The NLSEs for $\tilde{A}^{\pm}(z,\omega)$ are expressed as

$$\pm\partial_z\tilde{A}^{\pm}(z,\omega) = D^{\pm}(z,\omega) + N^{\pm}(z,\omega) + G^{\pm}(z,\omega) + f_{SE} \quad (1)$$

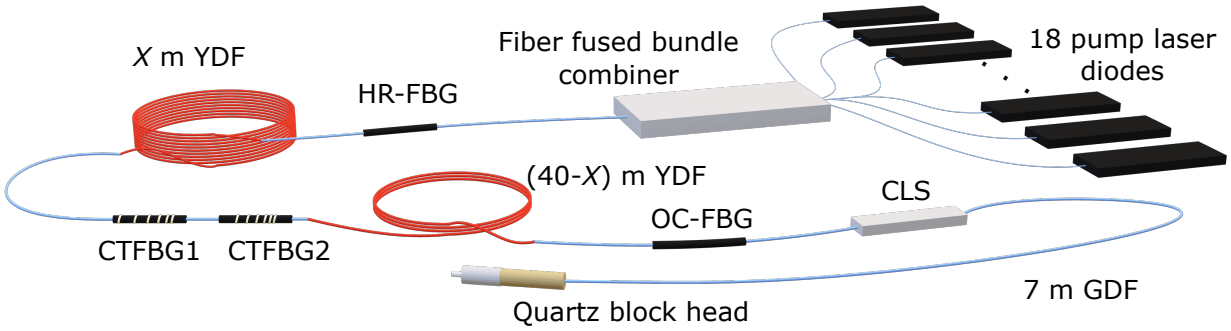

Figure 4: Schematic of the YDFL. HR-FBG: high-reflectance FBG. OC-FBG: output-coupler FBG. CLS: cladding light stripper. YDF: 20/400 μm Ytterbium-doped fiber, GDF: 20/400 μm Germanium-doped fiber.

where $D^{\pm}(z,\omega)$, $N^{\pm}(z,\omega)$, $G^{\pm}(z,\omega)$, and f_{SE} represent chromatic dispersion, nonlinear effects, active gain, and spontaneous emission noise terms, respectively. The dispersion term is calculated by

$$D^{\pm}(z,\omega) = i\sum_{n=1}^{3}\frac{\beta_n}{n!}\omega^n\tilde{A}^{\pm}(z,\omega) \tag{2}$$

where β_n is the n-th order derivative of the propagation constant. The nonlinear term is calculated by

$$N^{\pm}(z,\omega) = i\gamma(1+\frac{\omega}{\omega_0})F\{A^{\pm}(z,t)\cdot R(t)\otimes|A^{\pm}(z,t)|^2\} \tag{3}$$

where γ is the Kerr nonlinear coefficient, ω_0 is the carrier frequency of the signal, $F\{\cdot\}$ is the Fourier transform, $\otimes$ is the convolution operation, $h(t)$ is Raman response, which is fitted according to Ref. 30, and $R(t) = (1-f_R)\delta(t) + f_R h(t)$ is nonlinear response function, with $(1-f_R)\delta(t)$ accounted for the instantaneous electronic response and $f_R h(t)$ accounted for the retarded molecular responses [31], i.e. Raman response $h(t)$ considered here. The gain term is expressed as

$$G^{\pm}(z,\omega) = \frac{1}{2}(\Gamma_s[\sigma_a(\omega)+\sigma_e(\omega)]N_2(z) - \sigma_a(\omega)N_0)\tilde{A}^{\pm}(z,\omega) \tag{4}$$

which is dependent on the excited Yb-ion number $N_2(z)$, total Yb-ion number N_0, absorption/emission cross section σ_a/σ_e, and the overlap factor Γ_s between the signal light and the fiber core. In addition, the excited Yb-ion number $N_2(z)$ is related to the pump power $P_p(z)$ and governed by equations

$$\frac{d}{dz}P_p(z) = -\Gamma_p\{\sigma_a(\omega_p)N_0 - (\sigma_a(\omega_p)+\sigma_s(\omega_p))N_2(z)\} - \alpha_p P_p(z) \tag{5}$$

$$\frac{N_2}{N_0} = \{\frac{\Gamma_p}{\hbar\omega_p\mathcal{A}}\sigma_a(\omega_p)P_p + \frac{\Gamma_s}{2\pi T_m\mathcal{A}}\int\frac{\sigma_a(\omega)}{\hbar\omega}(|\tilde{A}^{+}|^2+|\tilde{A}^{-}|^2)d\omega\}/$$
$$\{\frac{\Gamma_p}{\hbar\omega_p\mathcal{A}}(\sigma_a(\omega_p)+\sigma_s(\omega_p))P_p + \frac{1}{\tau} + \frac{\Gamma_s}{2\pi T_m\mathcal{A}}\int\frac{\sigma_a(\omega)+\sigma_s(\omega)}{\hbar\omega}(|\tilde{A}^{+}|^2+|\tilde{A}^{-}|^2)d\omega\} \tag{6}$$

where Γ_p is the spatial overlap coefficient between pump light and the fiber core, ω_p is the pump light frequency, α_p is the passive loss of the active fiber at the pumping wavelength, T_m is the time window, τ is the excited state population lifetime, $\mathcal{A}$ is the doped cross-section area, and $\hbar$ is Plank's constant and is the doped cross-section area. Finally, the HR-FBG and OC-FBG form boundary conditions for the reciprocating propagation process

$$\tilde{A}^{+}(0,\omega) = \sqrt{R_{\mathrm{HR}}(\omega)}\tilde{A}^{-}(0,\omega) \tag{7}$$

$$\tilde{A}^{-}(L,\omega) = \sqrt{R_{\mathrm{OC}}(\omega)}\tilde{A}^{+}(L,\omega) \tag{8}$$

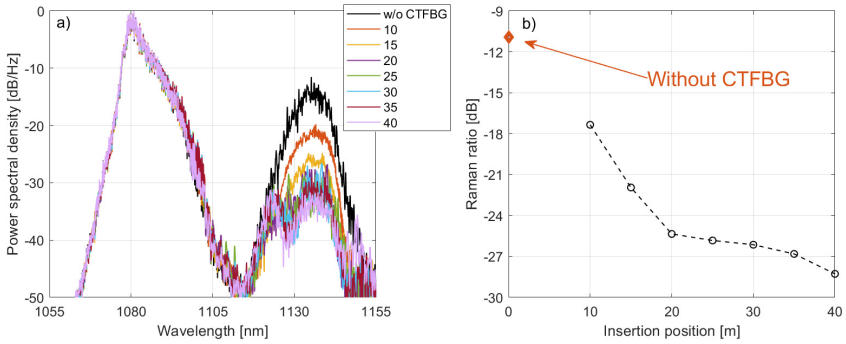

Figure 5: Simulation output spectra as a function of insertion position X, with a) X=10–40 m and without CTFBG, b) Raman ratio of output spectra as a function of insertion position.

where R_{HR} and R_{OC} are spectral reflectance coefficients of the HR-FBG and the OC-FBG, respectively. The field transmitted through the OC-FBG follows $\tilde{A}_{out} = \tilde{A}^{+}(L,\omega)\sqrt{1-R_{\mathrm{OC}}(\omega)}$, where L is the active fiber length. As well, the forward propagating field gets filtered by the CTFBG at position X following

$$\tilde{A}^{+}(X+\Delta z,\omega) = \tilde{A}^{+}(X,\omega)\sqrt{T_{\mathrm{CT}}(\omega)} \tag{9}$$

where $T_{\mathrm{CT}}(\omega)$ is the transmission spectrum of the CTFBG. Intracavity losses due to the insertion of the CTFBG are considered. They include two splices with a broadband loss of 0.1 dB per splice, a CTFBG transmission loss of 0.12 dB at wavelengths between 1075 to 1085 nm, and the filter transmission function $T_{\mathrm{CT}}(\omega)$. At the YDFL output, the CLS, delivery fiber, and QBH provide an additional broadband attenuation of 0.1 dB.

3.2. Modelling configurations

The HR-FBG reflectance coefficients R_{HR} and OC-FBG reflectance R_{OC} used in the modelling have Gaussian spectral profiles. R_{HR} has a bandwidth of 4 nm and a reflectance of 99%, and R_{OC} has a bandwidth of 1 nm and a reflectance of 10%. The transmission spectral profile of the CTFBG used in the modelling is attained by fitting the measured transmission profile of the CTFBG shown in Figure 3. Table 1 lists the main parameters used in the modelling. The rest of the parameters follows the parameters of 20/400 μm YDF reported in Ref. 29.

Table 1: Main parameters used in the simulation.

Name	Value	Name	Value	Name	Value	Name	Value
P_p [W]	2300	λ_s [nm]	1080	β_3 [ps^3/km]	0.04	Γ_s	0.85
L [m]	40	λ_p [nm]	915	β_2 [ps^2/km]	20.4	Γ_p	0.0024
τ [ms]	0.85	N_0 [$\times 10^{25}$m^{-3}]	4.262	γ [W^{-1}/km]	0.5	f_R	0.18

In the modelling, the CTFBG insertion position X varies from 10 m to 40 m by increments of 5 m. The output spectra and power filtered by the CTFBG are compared at different values of X. In particular, a Raman ratio is calculated to evaluate the power percentage of the SRS content inside the output light. Raman ratio is calculated via the laser output spectrum integrated from 1120 nm to 1160 nm divided by the laser output spectrum integrated from 1050 nm to 1160 nm [29].

3.3. Simulation results

Figure 5a) shows the simulation output spectra as a function of X, for the same pump power P_p=2300 W. The output spectrum without CTFBG has an SRS peak at -12 dB. When X increases from 10 m to 20 m, the SRS peak gradually drops, leading to an SRS peak at -28 dB when X=20 m. When X increases from 10 m to 40 m, the SRS peak gradually drops, leading to an SRS peak at -20 dB when X=20 m and even less for larger values of X. Figure 5b) shows the Raman ratio as a function of X. It is noticed that a larger X consistently leads to a smaller Raman ratio.

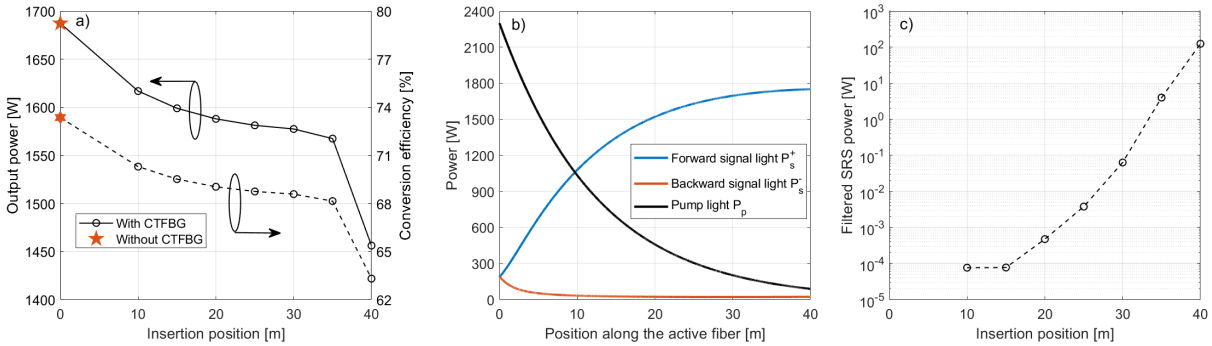

Figure 6: Modelling results. a) Output power and power conversion efficiency η as a function of insertion position X. b) Power distribution along the active fiber of pump light, forward propagating light and backward-propagating light. c) Filtered SRS power as a function of insertion position.

However, when the insertion position ≥20 m, difference between Raman ratios of the output spectra becomes small, e.g. the Raman ratio has merely been improved by 3 dB when X increases from 20 m to 40 m, in comparison to over 14 dB difference for X from 0 to 20 m.

Insertion positions also have an impact on the output power. Figure 6a) shows the output power and power conversion efficiency as a function of X, for the same pump power P_p=2300 W. The YDFL without CTFBG has an efficiency of 73%. After CTFBG insertion, the efficiency drops from 70.3% gradually to 68.6% as X increases from 10 to 30 m. The decrease of efficiency when X≤30 m is attributed to splice losses and transmission losses at signal wavelength caused by CTFBG. In the range of X≥35 m, the efficiency drops further steeply from 68.1% to 63.3%. Besides the splice losses and transmission losses, the power transfer to SRS light that subsequently becomes filtered out by the CTFBG leads to a significant decrease in efficiency when X≥35 m.

Figure 6b) shows the simulated power distribution of pump power (P_p), forward-propagating signal power (P_s^+), and backward-propagating signal power (P_s^-) along the active fiber without CTFBG. The injected pump power of 2300 W is absorbed along the active fiber and converted to the power of forward/backward propagating light. It is noted that at the boundary condition of the OC-FBG, the total reflected power is less than the 10% reflectivity of the OC-FBG because the forward spectrum exceeds the reflection spectrum of the OC-FBG. The power distribution is almost unchanged before and after inserting the CTFBG, but with a power loss at P_s^+ from the filtering of SRS light at the insertion position, i.e. the filtered SRS power caused by the CTFBG, splice losses, and transmission losses at signal wavelength. Figure 6c) compares the filtered SRS power as a function of insertion position X. It is shown that filtered SRS power increases gradually with the insertion position. When X≤30 m, filtered SRS power is <0.1 W and insignificant with respect to the total output power. When X=35 m, filtered SRS power is 4 W, and at X=40 m filtered SRS power is 104 W, leading to significant reduction in YDFL output power. These results show that when X increases, a stronger SRS content is generated in the forward propagating light prior to the SRS removal by the CTFBG. Therefore, a late insertion of the CTFBG leads to a significant loss in the output power.

Comparing Figure 5 and Figure 6, it appears that X=30 m is a judicious compromise in between Raman ratio and output YDFL power. On one hand, from Figure 5b), the Raman ratio when X=35 m or X=40 m is at best 2 dB better than the Raman ratio when X=30 m. On the other hand, from Figure 6a), a larger X leads to a gradual decrease in efficiency when X≤30 m, because of the intracavity splice loss and the insertion loss at signal wavelength from the CTFBG. However, the decrease in efficiency becomes fast when X>30 m, and steeply when X≥35 m. This steep decrease in efficiency results from the significant filtered SRS power, which can be seen from Figure 6c). Besides the factors of loss in efficiency, the significant filtered SRS power should be prevented for the factor of laser diode safety as well. Because the filtered SRS power is reflected backwardly in the cladding, a large filtered SRS power can enter the pump combiner and damage the laser diodes. Hence, X=30 m is chosen for the experimental configuration, i.e. the CTFBG divides the 40 m oscillator into a section of 30 m and a section of 10 m.

4. Experimental results

Figure 7a) shows output spectra of the YDFL with X=30 m as a function of YDFL output power. The SRS content is effectively suppressed when YDFL output power ≤1.88 kW. An SRS peak at a wavelength of 1124.5 nm emerges when the output power is 1.97 kW. This is caused by the short wavelength cutoff of CTFBG2, as shown in the transmission spectral profile in Figure 3. Figure 7b) shows the output power and the Raman ratio as a function of pump power. The YDFL has a power conversion efficiency of 68%. In reference to our previous work of Ref. 24, the YDFL without CTFBG has a power conversion efficiency of 73%. The decrease in efficiency from 73% to 68% matches the simulation results of Figure 6a). The decrease in efficiency is caused by splice losses and transmission losses of the CTFBG at signal wavelength.

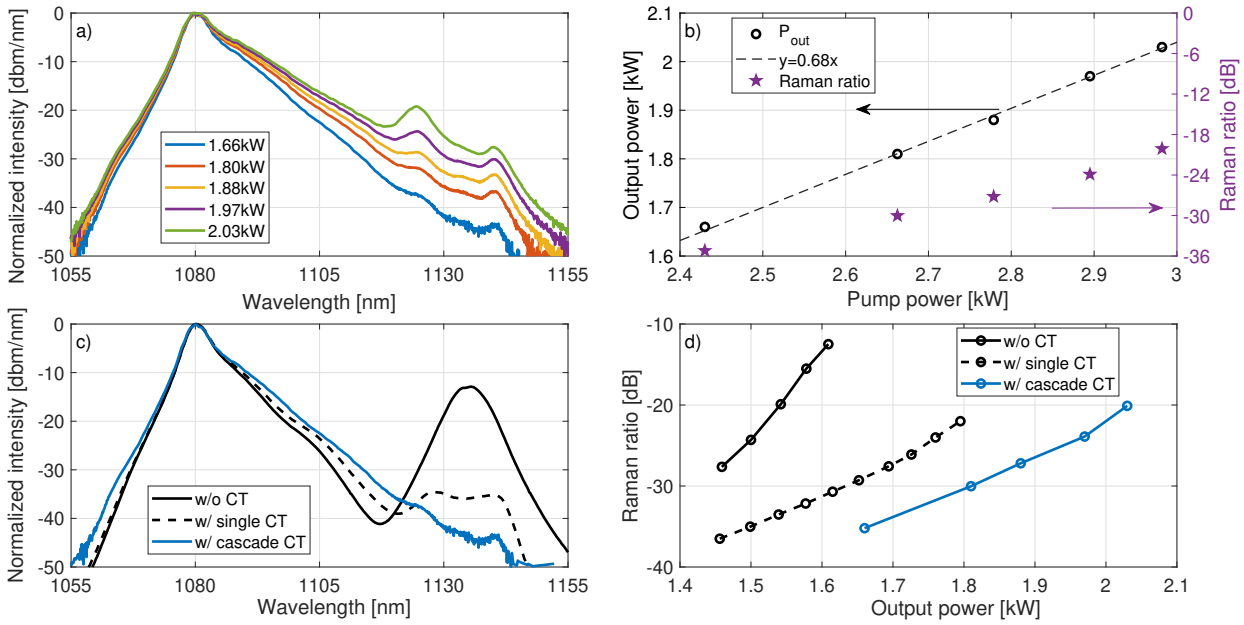

Figure 7: Result of the YDFL with X = 30. a) Output spectra as a function of output power. b) Output power and Raman ratio as a function of pump power. c) Output spectra of the YDFL at an output power of 1.6 kW without a CTFBG (w/o CT, data from Ref. 24), with a single CTFBG (c/ single CT, data from Ref. 24), and with a cascaded CTFBG (w/ cascade CT). d) Raman ratio as a function of output power of YDFL w/o CT, w/ single CT, and w/ cascade CT.

From Figure 7b), the Raman ratio grows steadily from -35.2 dB at the output power of 1.66 kW to -20.1 dB at the output power of 2.03 kW. The beam quality of the output laser is measured according to the standard method ISO 11146, with the use of a focal lens and a commercial beam analyzer produced by PRIMES (FocusMonitor). The beam quality is M^2=1.37 at the output power of 1.81 kW. Beam quality measurement at larger output power is prevented by the damage threshold of the measurement system.

In our previous work of Ref. 24, the output spectra were compared before/after a single CTFBG was inserted at the position of X=30 m inside a 40 m YDFL. The output spectra from Ref. 24 are used as reference to compare with the experimental result in this paper. Figure 7c) compares the output spectra of the 40 m YDFL without the insertion of a CTFBG (w/o CT), with the intracavity insertion of a single strand of CTFBG (w/ single CT), and with the intracavity insertion of the cascaded CTFBG (w/ cascade CT). For the three YDFL set at the output power of 1.6 kW, the YDFL without a CTFBG has the strongest SRS peak. With a single CTFBG, the SRS is mitigated compared to the YDFL without a CTFBG. However, an SRS peak still emerges in the wavelength range of 1127–1141 nm, because the SRS spectrum exceeds the single CTFBG spectral range Finally, no significant SRS peak has emerged with the cascade CTFBG. Therefore, the cascaded CTFBG effectively suppresses the SRS. Figure 7d) compares the Raman ratio as a function of output power of the YDFL without a CTFBG, with a single strand of CTFBG, and with the cascade CTFBG. The results show that the YDFL without a CTFBG has P_{th}=1.54 kW. The intracavity insertion of

the single CTFBG improves P_{th} to 1.80 kW, and the intracavity insertion of the cascaded CTFBG further improves P_{th} to 2.03 kW.

The cascaded CTFBG is placed on a V-groove for heat dissipation. A thermal camera (FLIR) is used to monitor the temperature of the cascaded CTFBGs. Figure 8a) and Figure 8b) show thermal images of temperature elevation ΔT of CTFBG1 and CTFBG2, respectively, when the YDFL output power reaches 2.03 kW. Figure 8c) and Figure 8d) quantitatively present ΔT as a function of YDFL output power along the fiber axis at the CTFBG locations. It is noticed that ripples appear on the thermal profiles along the fiber axes, e.g. position ~2.7 cm in Figure 8c) and position from 1.2 cm to 2 cm in Figure 8d). These ripples and spikes result from the local contamination spots in the recoating area. Figure 9 shows the maximum temperature elevation ΔT_{max} of CTFBGs as a function of YDFL output power. It is found that ΔT_{max} of each CTFBG grows proportionally with the pump power, with the growth rate ~30.6 °C/kW for CTFBG1 and ~15.6 °C/kW for CTFBG2. The ΔT_{max} for CTFBG1 reaches 85°C at the maximum power. It is believed that the different temperature growth rates of CTFBG1 and CTFBG2 result from the different UV-laser exposure time during CTFBG inscription. In the future, the thermal handling capacity of CTFBGs could be improved with a better design of cascaded CTFBGs, for example by distributing the heat load on multiplexed CTFBGs, as demonstrated in Ref. 32.

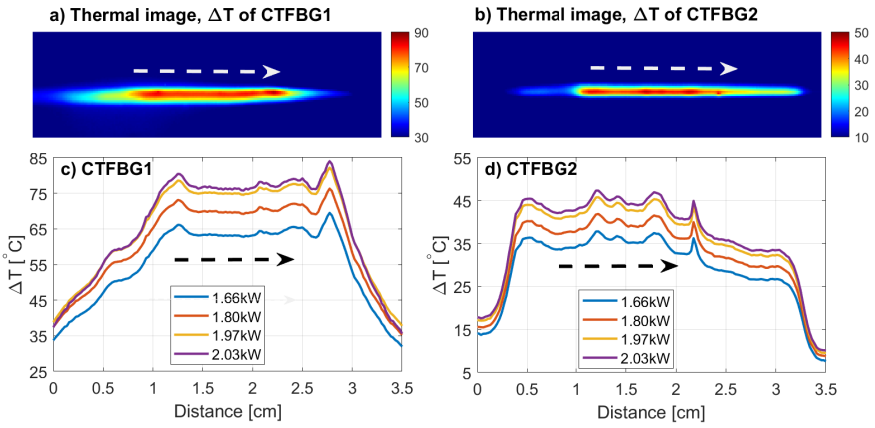

Figure 8: Thermal image of the temperature elevation ΔT (YDFL output power = 2.03 kW) of a) CTFBG1 and b) CTFBG2. ΔT along fiber axis as a function of YDFL output power of c) CTFBG1 and d) CTFBG2. Arrows indicate the directions of forward propagating light in the oscillator.

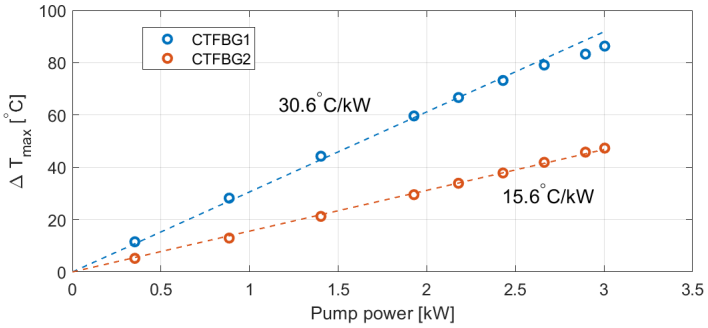

Figure 9: Maximum temperature elevation ΔT_{max} of CTFBGs as a function of YDFL output power.

5. Conclusion

In conclusion, thanks to the SRS suppression from a 21.1 nm spectrally broad CTFBG, the first 2 kW monolithic YDFL based on 20 μm-core double-cladding fibers and 915 nm pump source has been reported. The CTFBG insertion

position of X=30 meters is optimized by a numerical modelling based on NLSE, and results from a compromise in between SRS suppression and YDFL output power. Compared to a single intra-cavity CTFBG with a 10 nm bandwidth and -13 dB transmission depth reported in a previous work, the proposed cascaded CTFBG enhances the Raman threshold of a monolithic YDFL from 1.8 kW to 2.03 kW. This YDFL is of high commercial relevance because of the combined simplicity of its design and high output power.

Acknowledgement A portion of this content was presented at the Advanced Solid State Lasers Conference [33].

Disclosures The authors declare no conflicts of interest.

References

[1] D. J. Richardson, J. Nilsson, W. A. Clarkson, High power fiber lasers: current status and future perspectives, JOSA B 27 (11) (2010) B63–B92.
[2] Y. Xiao, F. Brunet, M. Kanskar, M. Faucher, A. Wetter, N. Holehouse, 1-kilowatt cw all-fiber laser oscillator pumped with wavelength-beam-combined diode stacks, Optics express 20 (3) (2012) 3296–3301.
[3] P. Barua, E. Sekiya, K. Saito, A. Ikushima, Influences of yb3+ ion concentration on the spectroscopic properties of silica glass, Journal of non-crystalline solids 354 (42-44) (2008) 4760–4764.
[4] J. Koponen, M. Söderlund, H. J. Hoffman, D. A. Kliner, J. P. Koplow, M. Hotoleanu, Photodarkening rate in yb-doped silica fibers, Applied optics 47 (9) (2008) 1247–1256.
[5] A. Guzman Chavez, A. Kir'Yanov, Y. O. Barmenkov, N. Il'Ichev, Reversible photo-darkening and resonant photobleaching of ytterbium-doped silica fiber at in-core 977-nm and 543-nm irradiation, Laser Physics Letters 4 (10) (2007) 734–739.
[6] Y. Huang, Q. Xiao, D. Li, J. Xin, Z. Wang, J. Tian, Y. Wu, M. Gong, L. Zhu, P. Yan, 3 kw narrow linewidth high spectral density continuous wave fiber laser based on fiber bragg grating, Optics & Laser Technology 133 (2021) 106538.
[7] B. Volodin, S. Dolgy, E. Melnik, E. Downs, J. Shaw, V. Ban, Wavelength stabilization and spectrum narrowing of high-power multimode laser diodes and arrays by use of volume bragg gratings, Optics letters 29 (16) (2004) 1891–1893.
[8] C. Giles, T. Erdogan, V. Mizrahi, Simultaneous wavelength-stabilization of 980-nm pump lasers, in: Optical Amplifiers and Their Applications, Optical Society of America, 1993, p. PD11.
[9] B. Dahmani, L. Hollberg, R. Drullinger, Frequency stabilization of semiconductor lasers by resonant optical feedback, Optics letters 12 (11) (1987) 876–878.
[10] S. Klein, M. Giesberts, M. Traub, O. Fitzau, D. Hoffmann, Frequency stabilization of multimode diode lasers with fiber bragg gratings, in: 2019 IEEE High Power Diode Lasers and Systems Conference (HPD), IEEE, 2019, pp. 21–22.
[11] M. Niebuhr, C. Zink, A. Jechow, A. Heuer, L. B. Glebov, R. Menzel, Mode stabilization of a laterally structured broad area diode laser using an external volume bragg grating, Optics express 23 (9) (2015) 12394–12400.
[12] B. Yang, H. Zhang, X. Wang, R. Su, R. Tao, P. Zhou, X. Xu, Q. Lu, Mitigating transverse mode instability in a single-end pumped all-fiber laser oscillator with a scaling power of up to 2 kw, Journal of Optics 18 (10) (2016) 105803.
[13] F. Zhang, W. Zheng, P. Shi, X. Zhang, 2-kw single-mode fiber laser employing bidirectional-pump scheme, in: 2017 International Conference on Optical Instruments and Technology: Advanced Laser Technology and Applications, Vol. 10619, International Society for Optics and Photonics, 2018, p. 106190G.
[14] B. Yang, H. Zhang, C. Shi, R. Tao, R. Su, P. Ma, X. Wang, P. Zhou, X. Xu, Q. Lu, 3.05 kw monolithic fiber laser oscillator with simultaneous optimizations of stimulated raman scattering and transverse mode instability, Journal of Optics 20 (2) (2018) 025802.
[15] H. Yu, X. Wang, R. Tao, P. Zhou, J. Chen, 1.5 kw, near-diffraction-limited, high-efficiency, single-end-pumped all-fiber-integrated laser oscillator, Applied optics 53 (34) (2014) 8055–8059.
[16] K. Hejaz, M. Shayganmanesh, A. Roohforouz, R. Rezaei-Nasirabad, A. Abedinajafi, S. Azizi, V. Vatani, Transverse mode instability threshold enhancement in yb-doped fiber lasers by cavity modification, Applied optics 57 (21) (2018) 5992–5997.
[17] V. Distler, F. Möller, M. Strecker, G. Palma-Vega, T. Walbaum, T. Schreiber, Transverse mode instability in a passive fiber induced by stimulated raman scattering, Optics Express 28 (15) (2020) 22819–22828.
[18] F. Liu, T. Guo, C. Wu, B.-O. Guan, C. Lu, H.-Y. Tam, J. Albert, Wideband-adjustable reflection-suppressed rejection filters using chirped and tilted fiber gratings, Optics express 22 (20) (2014) 24430–24438.
[19] E. Kuzin, G. Beltran-Perez, M. Basurto-Pensado, R. Rojas-Laguna, J. Andrade-Lucio, M. Torres-Cisneros, E. Alvarado-Mendez, Stimulated raman scattering in a fiber with bending loss, Optics communications 169 (1-6) (1999) 87–91.
[20] C. Shi, R. T. Su, H. W. Zhang, B. L. Yang, X. L. Wang, P. Zhou, X. J. Xu, Q. S. Lu, Experimental study of output characteristics of bi-directional pumping high power fiber amplifier in different pumping schemes, IEEE Photonics Journal 9 (3) (2017) 1–10.
[21] M. Wang, Z. Li, L. Liu, Z. Wang, X. Gu, X. Xu, Fabrication of chirped and tilted fiber bragg gratings on large-mode-area doubled-cladding fibers by phase-mask technique, Applied optics 57 (16) (2018) 4376–4380.
[22] M. Wang, Z. Wang, L. Liu, Q. Hu, H. Xiao, X. Xu, Effective suppression of stimulated raman scattering in half 10 kw tandem pumping fiber lasers using chirped and tilted fiber bragg gratings, Photonics Research 7 (2) (2019) 167–171.
[23] K. Jiao, J. Shu, H. Shen, Z. Guan, F. Yang, R. Zhu, Fabrication of kw-level chirped and tilted fiber bragg gratings and filtering of stimulated raman scattering in high-power cw oscillators, High Power Laser Science and Engineering 7.
[24] W. Lin, M. Desjardins-Carrière, B. Sévigny, J. Magné, M. Rochette, Raman suppression within the gain fiber of high-power fiber lasers, Applied Optics 59 (31) (2020) 9660–9666.
[25] X. Tian, X. Zhao, M. Wang, Z. Wang, Effective suppression of stimulated raman scattering in direct laser diode pumped 5 kilowatt fiber amplifier using chirped and tilted fiber bragg gratings, Laser Physics Letters 17 (8) (2020) 085104.
[26] X. Zhao, X. Tian, M. Wang, H. Li, B. Rao, Z. Wang, Design and fabrication of wideband chirped tilted fiber bragg gratings, Optics & Laser Technology 148 (2022) 107790.

[27] B. Rao, X. Zhao, H. Li, X. Tian, M. Wang, Z. Wang, Mode coupling in large-mode-area double-cladding chirped and tilted fiber bragg gratings, Optics Express 29 (7) (2021) 11277–11292.
[28] X. Tian, X. Zhao, M. Wang, Q. Hu, H. Li, B. Rao, H. Xiao, Z. Wang, Influence of bragg reflection of chirped tilted fiber bragg grating on raman suppression in high-power tandem pumping fiber amplifiers, Optics Express 28 (13) (2020) 19508–19517.
[29] W. Liu, P. Ma, H. Lv, J. Xu, P. Zhou, Z. Jiang, General analysis of srs-limited high-power fiber lasers and design strategy, Optics express 24 (23) (2016) 26715–26721.
[30] D. Hollenbeck, C. D. Cantrell, Multiple-vibrational-mode model for fiber-optic raman gain spectrum and response function, JOSA B 19 (12) (2002) 2886–2892.
[31] Q. Lin, G. P. Agrawal, Raman response function for silica fibers, Optics letters 31 (21) (2006) 3086–3088.
[32] H. Song, D. Yan, W. Wu, B. Shen, X. Feng, Y. liu, L. Li, Q. Chu, M. Li, J. Wang, R. Tao, SRS suppression in multi-kw fiber lasers with a multiplexed ctfbg, Opt. Express 29 (13) (2021) 20535–20544. doi:10.1364/OE.426979.
URL http://www.osapublishing.org/oe/abstract.cfm?URI=oe-29-13-20535
[33] W. Lin, M. Desjardins-Carrière, V. L. Iezzi, A. Vincelette, M.-H. Bussières-Hersir, M. Rochette, 2 kw fiber laser based on 20 μm-core double-cladding fibers and 915 nm pump sources, in: Advanced Solid State Lasers, Optical Society of America, 2021, p. JM3A.24.
URL http://www.osapublishing.org/abstract.cfm?URI=ASSL-2021-JM3A.24